
Article:
Venkat, G. orcid.org/0000-0001-6255-3151, Vidamour, I. orcid.org/0000-0002-6909-2711, Swindells, C. orcid.org/0000-0002-9572-5930 et al. (8 more authors) (2024) Exploring physical and digital architectures in magnetic nanoring array reservoir computers. Neuromorphic Computing and Engineering, 4 (2). 024018. ISSN 2634-4386

https://doi.org/10.1088/2634-4386/ad53f9

Exploring physical and digital architectures in magnetic nanoring array reservoir computers

NEUROMORPHIC
Computing and Engineering

OPEN ACCESS

RECEIVED
12 December 2023

REVISED
15 April 2024

ACCEPTED FOR PUBLICATION
4 June 2024

PUBLISHED
27 June 2024

PAPER

Exploring physical and digital architectures in magnetic nanoring array reservoir computers

G Venkat[1], I T Vidamour[1,2], C Swindells[1], P W Fry[3], M C Rosamond[4], M Foerster[5], M A Niño[5], D Griffin[6], S Stepney[6], D A Allwood[1] and T J Hayward[1,*]

[1] Department of Materials Science and Engineering, University of Sheffield, Sheffield S1 3JD, United Kingdom
[2] Department of Computer Science, University of Sheffield, Sheffield S1 4DP, United Kingdom
[3] Nanoscience and Technology Centre, University of Sheffield, Sheffield S3 7HQ, United Kingdom
[4] School of Electronic and Electrical Engineering, University of Leeds, Leeds LS2 9JT, United Kingdom
[5] ALBA Synchrotron Light Facility, 08290 Cerdanyola del Valles, Spain
[6] Department of Computer Science, University of York, York YO10 5GH, United Kingdom
[*] Author to whom any correspondence should be addressed.

E-mail: t.hayward@sheffield.ac.uk

Keywords: reservoir computing, machine learning, magnetic domain wall devices

Supplementary material for this article is available online

Abstract

Physical reservoir computing (RC) is a machine learning technique that is ideal for processing of time dependent data series. It is also uniquely well-aligned to *in materio* computing realisations that allow the inherent memory and non-linear responses of functional materials to be directly exploited for computation. We have previously shown that square arrays of interconnected magnetic nanorings are attractive candidates for *in materio* RC, and experimentally demonstrated their strong performance in a range of benchmark tasks (Dawidek *et al* 2021 *Adv. Funct. Mater.* **31** 2008389, Vidamour *et al* 2022 *Nanotechnology* **33** 485203, Vidamour *et al* 2023 *Commun. Phys.* **6** 230). Here, we extend these studies to other lattice arrangements of rings, including trigonal and Kagome grids, to explore how these affect both the magnetic behaviours of the arrays, and their computational properties. We show that while lattice geometry substantially affects the microstate behaviour of the arrays, these differences manifest less profoundly when averaging magnetic behaviour across the arrays. Consequently the computational properties (as measured using task agnostic metrics) of devices with a single electrical readout are found to be only subtly different, with the approach used to time-multiplex data into and out of the arrays having a stronger effect on properties than the lattice geometry. However, we also find that hybrid reservoirs that combine the outputs from arrays with different lattice geometries show enhanced computational properties compared to any single array.

1. Introduction

Neuromorphic computing is being actively pursued for artificial intelligence and machine learning applications and investment in it is projected to grow significantly in the coming decade [1]. However, the cost associated with training large neural networks for such applications can be significant and this has led to investigation into unconventional computing approaches with lower energy footprints.

Reservoir computing [2–4] (RC) is a computing paradigm which uses the dynamics of a recurrent neural network (RNN) or another dynamical system (algorithmic or physical), often referred to as the reservoir, to transform input data to a higher dimensional space where it may be classified more easily. It has attracted interest in recent years mainly because the internal weights of the RNN are fixed and hence do not need to be trained, creating substantial energy savings when compared to a conventional RNN [5]. Significantly, the 'black-box' nature of the reservoir means that the RNN can be replaced by any dynamical system that has (a) a non-linear response to stimuli, (b) a state space rich enough to allow input data to be expanded into higher

dimensional space where classification becomes easier and (c) an asymptotic washing out of system states with stimuli (typically refered to as 'fading memory'). This has led to a wide variety of different implementations of *in materia* RC using e.g. photonic [6], mechanical [7] and memristive [8, 9] systems.

In-materia RC offers potential advantages of increased computational efficiency in temporal tasks compared to other static *in materio* computing paradigms which resemble standard neural networks. Here the material acts simply as a nonlinear activation function and consequently *in-materia* RC can even compete in performance with *in silico* computing approaches [10]. Benchmark tasks demonstrated using RC approaches include signal transformation, speech and image recognition and time series prediction [11–14].

Reservoirs need to have different computational properties to be effective in different tasks. For example, tasks such as signal transformation and spoken digit recognition primarily utilise the non-linear transform provided by the reservoir, while the well-known NARMA-10 task requires the reservoir to provide both non-linearity and memory of past inputs [11].

There are mainly two ways to tune an *in materio* reservoir's properties: Firstly, intrinsic dynamics of the reservoir can be changed e.g. by making changes to the physical system used or by replacing it with another system altogether. For example, it has been reported that magnetic nanodots [15] and artificial spin ice [16, 17] systems exhibit different computational properties when their lattice arrangements are varied. Alternatively, the reservoir architecture (i.e. the way data is interfaced with the reservoir) can be changed, for example by using different time-multiplexing approaches [11]. However, the relative effectiveness of these two tuning approaches have yet to be explicitly compared for a given type of physical system.

We have previously shown that magnetic domain wall (MDW) dynamics in interconnected arrays of $Ni_{80}Fe_{20}$ (Permalloy) magnetic nanoring arrays (NRAs) can be exploited for RC [11, 18, 19]. In those studies, information was encoded in the amplitude of rotating applied magnetic fields, which then drove emergent DW interactions within the arrays. We have shown that the magnetic response of the arrays exhibited both the non-linearity and fading memory required for a useful reservoir, and demonstrated state-of-the-art performance for several benchmark tasks, including signal transformation, spoken digit recognition and time series prediction.

In this paper we explore how variations in the lattice arrangement of NRAs change both their physical behaviours, and their resulting computational properties when used as reservoirs. We study these alongside three different time-multiplexed RC architectures [11] to understand how the effects of changing the physical form of the reservoirs compare to those produced by changing the way we interface data with them.

We consider three different NRA lattices (refer to figure 1) with different numbers of nearest neighbours (NN) which directly overlap with a given ring: (a) square (with NN = 4), (b) trigonal (with NN = 6) and (c) Kagome (with NN = 3). We first use X-ray photo-emission electron microscopy (X-PEEM) imaging of the arrays' microstates to show that the different lattices exhibit different characteristic configurations of MDWs and differing evolutions of state with applied stimulus strength, thus showing the strong influence of the number and position of NN rings on NRA behaviour. We then use anisotropic magnetoresistance measurements (AMR) to probe the global responses of each NRA lattice arrangement, and use these with the three reservoir architectures to evaluate task agnostic metrics that quantify their computational properties. We observe that the time-multiplexing approach has a more profound influence on computational properties than the type of NRA lattice used, suggesting that our global readout mechanism does not allow differences in the rich microstate behaviours of the arrays to be fully captured. However, reservoirs constructed using the combined outputs of NRAs with different lattice arrangements do show enhanced computational metrics compared to reservoirs constructed from a single NRA, indicating the utility of combining the dynamics of multiple material reservoirs for improved computational performance.

2. Methodology

Each NRA had rings of diameter 4 μm and ring widths of 300–400 nm. The overlap between rings was 150–200 nm. The total area of each array was fixed at $\sim$100 μm^2. Figures 1(a)–(c) shows scanning electron microscopy (SEM) images of example arrays with square, trigonal and Kagome lattices respectively.

NRAs were patterned using electron beam lithography with lift-off processing. After electron beam exposure and development, 10 nm of $Ni_{80}Fe_{20}$ was thermally (AMR measurements) or electron beam (XPEEM measurements) evaporated before lift-off. Our previous studies have shown no appreciable difference in the magnetic field driven responses of thermally and electron beam evaporated ring arrays. The samples used for AMR measurements were patterned on thermally oxidised silicon substrates and underwent a second stage of lithography and metalisation to pattern Ti(20 nm)/Au(100 nm) electrical contacts at the edges of the NRAs (figure 5(b)). The samples for X-PEEM measurements were patterned on silicon substrates with native oxide layers and had an additional $\sim$2 nm Aluminium capping layer to avoid charging of the samples during X-PEEM imaging.

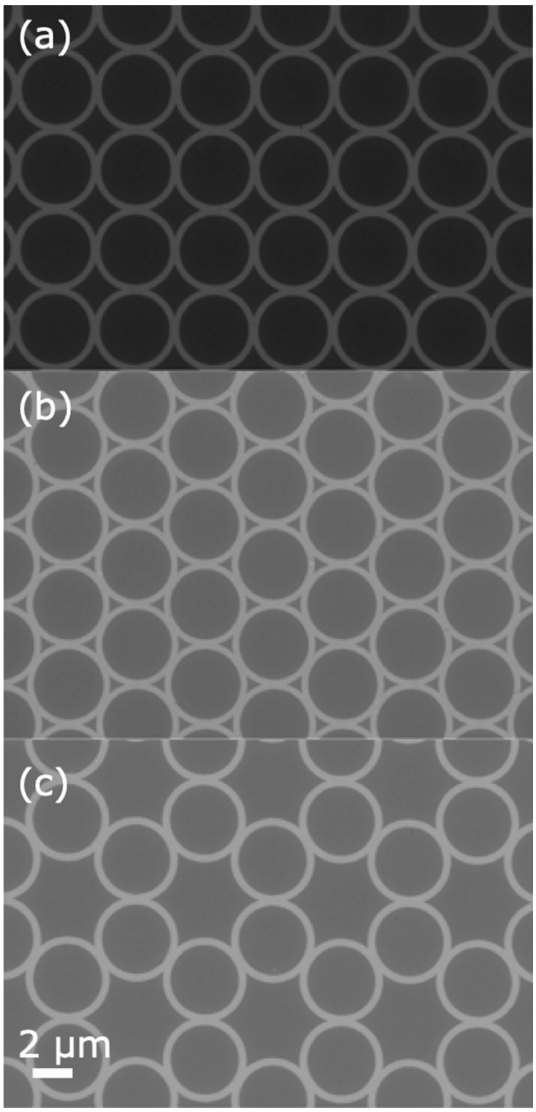

Figure 1. SEM images of ring arrays with (a) square, (b) trigonal and (c) Kagome lattice arrangements.

AMR measurements were performed using a custom-built electrical transport measurement rig. A sinusoidal probe current of 1 mA was provided to the NRA contacts at a frequency of 43 117 Hz using a Keithley 6221 current source. Resistance changes due to AMR effects [20, 21] were measured using a Stanford Research Model SR830 lock-in amplifier. Rotating magnetic fields at a frequency of 19 Hz were generated using two pairs of air-coil electromagnets in Helmholtz-like configurations. The electromagnets were driven by a pair of Kepco BOP 36-6D power supplies and were controlled with voltage signals supplied by a National Instrument acquisition card.

X-PEEM was performed at the CIRCE beamline at the ALBA synchrotron. Magnetic domains images were obtained by averaging a series of x-ray absorption images on and off the Fe-L_3 resonance with left and right x-ray circular polarization in order to generate contrast by x-ray magnetic circular dichroism. Samples were mounted on cartridges with a quadrupole magnet [22], which was used to generate in-plane rotating magnetic field at a frequency of 1 Hz. Microstate populations were extracted from the X-PEEM micrographs by using custom Python-based image processing libraries [23] to identify the magnetic configuration of each ring, and counting the number of each microstate configuration across the array. Confidence intervals for the state populations were calculated by measuring standard deviations of the counts of each state over three runs of the each measurement. The net magnetisation of the array was calculated by finding the weighted sum of the magnetisation components along the PEEM sensitivity direction for the relative population of different magnetic states.

In order to provide a more complete assessment of the range of computational behaviours available to a given reservoir, we employed task agnostic metrics to characterise the different lattice arrangements' computational properties instead of optimising the reservoirs to perform a specific task. We used the metrics

computational quality (CQ), which was evaluated from the kernel rank (KR) and generalisation rank (GR) [24, 25] and linear memory capacity (MC) [26] to evaluate the computational properties of a reservoir along two different axes using randomly generated data. These have been shown to be good predictors of task performance [25]. For full details on the implementation of each of the metrics, refer to the Supplementary material.

The metrics of KR and GR were evaluated similarly but measured opposite properties. Both evaluated the number of linearly independent output states when driven with uncorrelated (KR)/correlated inputs (GR). This measured the reservoir's ability to separate distinct input sequences (KR), as well as generalise similar inputs (GR). Both metrics were bounded by the number of output nodes the reservoir has. A system with good separation properties will have a high KR, while a system with good generalisation properties will have a low GR. CQ = KR-GR [27] is thus a basic heuristic and is an approximate measure of the classification ability of a physical reservoir. For a given application, the specific KR/GR values associated with ideal reservoir performance is highly dependent upon the task data. For example, a task which requires grouping of noisy repetitions of similar inputs to the same class requires a low GR value, while tasks which require seemingly similar inputs to be mapped to different output classes require high KR. A more extensive study into correlation between metrics and task performance can be found in [25].

Another important property of reservoir computers is their ability to retain information on past inputs. To measure this, MC evaluates how well the reservoir is able to reconstruct past inputs from its current reservoir state using a linear output layer. To do this, the readout layer of the reservoir was trained to reproduce delayed states over an input signal, then evaluated on an unseen test set. Again, MC was bounded by the number of output nodes in the network.

To explore the full range of dynamic regimes of the NRA, and hence measure the different computational properties of each regime, the input data was scaled to cover different ranges of the NRA's response. Each input datum $\boldsymbol{u}_\tau$ was encoded into the amplitude of a single rotation of the global rotating field at a frequency of 37 Hz. The encoding was linear and of the form $H_{\text{rot}} = H_{\text{c}} + H_{\text{r}} \times \boldsymbol{u}_\tau$, where H_{c} is the centre field and H_{r} is field range of the transformation (or input scaling parameters).

Previous work has shown that the full range of computational properties available to a given material cannot be accessed under a single time multiplexed reservoir architecture, since different architectures are able to better able to exploit given dynamic properties of a system's response for computational advantage [11]. Hence, it is important to test a range of different architectures in order to explore the full range of computational behaviours a given system can exhibit. Here we explore three reservoir architectures: the signal sub-sample reservoir (SSR), the single dynamical node reservoir (SDN), and the rotating neurons reservoir (RNR). The following section provides a phenomenological overview of each of the reservoir architectures. For further details on implementation, see supplementary material or [11].

The SSR architecture harnesses the oscillatory dynamics of the NRAs' electrical response. Due to the different nonlinear relationships between field and the different frequency components in the AMR signal, the shape of the AMR trace for a given rotation changes drastically according to field strength. When taking the amplitude of signal at multiple fixed points within the field rotation as output, both nonlinearity and dimensionality expansion is provided.

The SDN architecture, introduced by Appeltant *et al* [28], utilises the transient behaviours of the dynamic system to transform input data. The network consists of a single node (here, a single NRA) multiplexed in time, generating 'virtual' nodes. A fixed random mask provides different linear combinations of input dimensions to each virtual node, which are are connected to one another sequentially via the dependence of current system state on its past states. Again, both nonlinearity and dimensionality expansion are provided, plus the ability for the multiple dimensions of input data to interact with each other across time to form a richer representation.

Introduced by Liang *et al* [29], the RNR architecture employs multiple dynamical nodes unconnected from one another (here, each node is an isolated NRA). Instead, the input and output connections to each node synchronously rotate, which changes the input/output weights associated with each node over time. Considering the time series of a given output dimension, the output will have contributions from different nodes over time, emulating connections between nodes. By distributing information across the many real nodes, coupled with each node's inherent non-volatile response described in [11], information can stay in the system for long periods of time, enhancing memory.

3. Results and discussion

3.1. Microstate characterisation

We begin by studying the differences between the microstates formed in NRAs with different lattice arrangements (figure 2). In the X-PEEM measurements, the rings were first saturated and then 30 cycles of

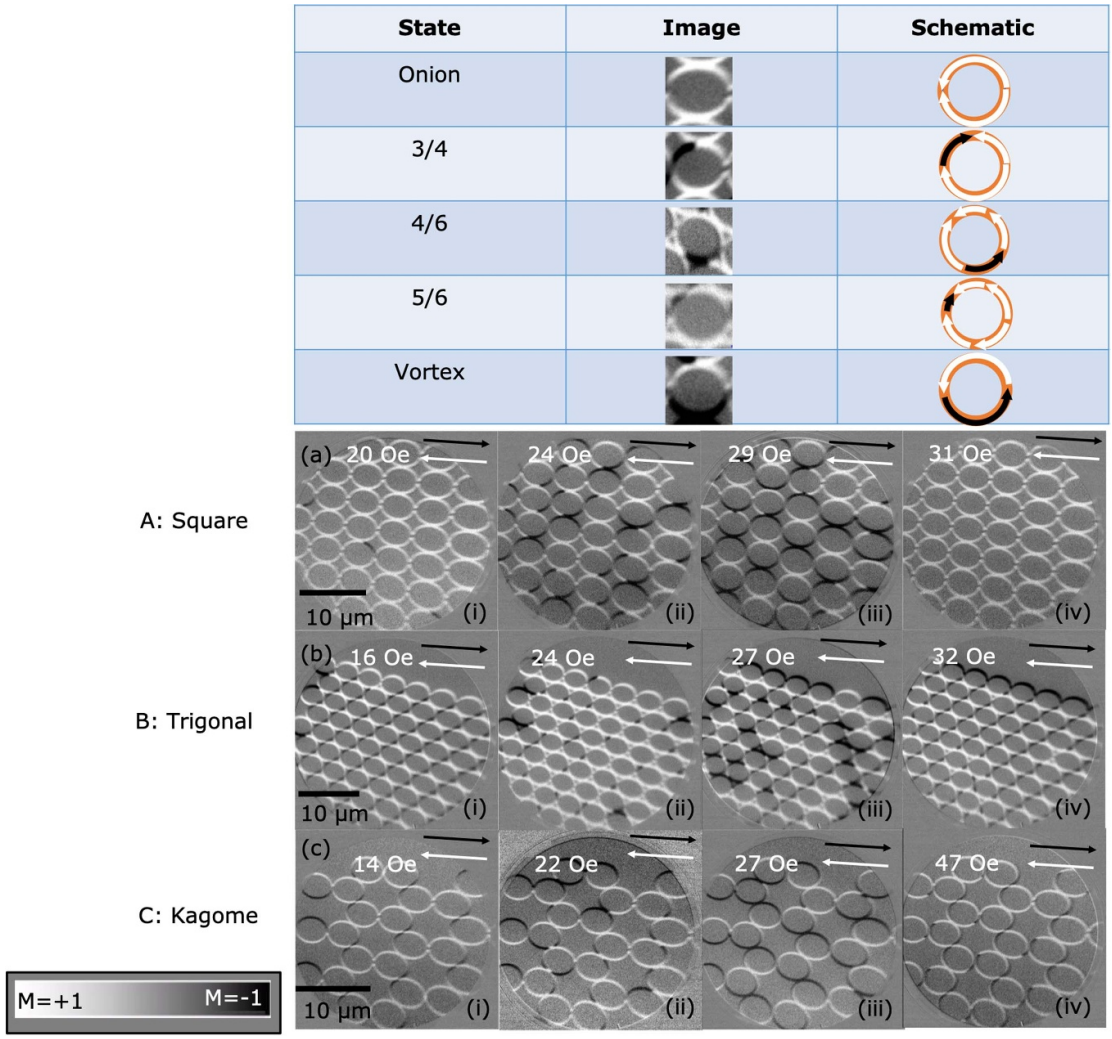

Figure 2. The X-PEEM responses for the (A) square, (B) trigonal and (C) Kagome lattice arrangements for as the rotating field amplitude was increased ((i)–(iv)). The table specified types of magnetic states seen in the different arrays along with schematics as well as representative images.

rotating fields of different amplitudes were applied with images subsequently being taken. As MDWs in the NRAs tend to pin in the junctions between rings, and these junction points differ in number and position between the three lattice-types, we defined a set of states in the table in figure 2. Here, we refer to three different types of domain microstates: the 'onion' microstate which reflects a pair of domain walls at opposite ends of the ring, and hence maximum net magnetisation in the direction of the domain walls, 'fractional' microstates which represents a variant of the 'onion' state in which a single MDW has shifted within the ring (with the fraction denoting the relative size of the larger domain in the ring), and the 'vortex' microstate with no domain walls and flux closure within the ring.

Figure 2(a) presents example microstates observed in the square lattice as a function of rotating field amplitude. At $H_{\mathrm{rot}} = 20$ Oe the field was too weak to depin MDWs from the junctions within which they were initialised, and hence all rings were in bi-domain states ('onion' states [30]), with net magnetisation aligned along the direction of initial saturation (figure 2(i)). At $H_{\mathrm{rot}} = 24$ Oe the field became strong enough to cause occasional MDW movement in some rings, thus forming '3/4' states with individual MDWs rotated by 90° from their initial position (figure 2(a-ii)). As the field was increased to $H_{\mathrm{rot}} = 29$ Oe, stochastic MDW depinning events increased in frequency, leading to MDW pairs colliding and annihilating to form flux-closed 'vortex' states (figure 2(a-iii)). We note that the ground state of a square-lattice NRA is a checker-board pattern of 'vortex' states with alternating circulation direction, but this is not typically reached due to the re-nucleation of MDWs pairs into 'vortex' states by MDW activity in neighbouring rings. Full details of these emergent effects can be found in our previous work [18]. At higher fields still ($H_{\mathrm{rot}} = 29 - 31$ Oe) large numbers of MDWs were active, meaning that MDW re-nucleation events dominated over annihilation events, and the array progressively repopulated with MDWs. By $H_{\mathrm{rot}} = 31$ Oe

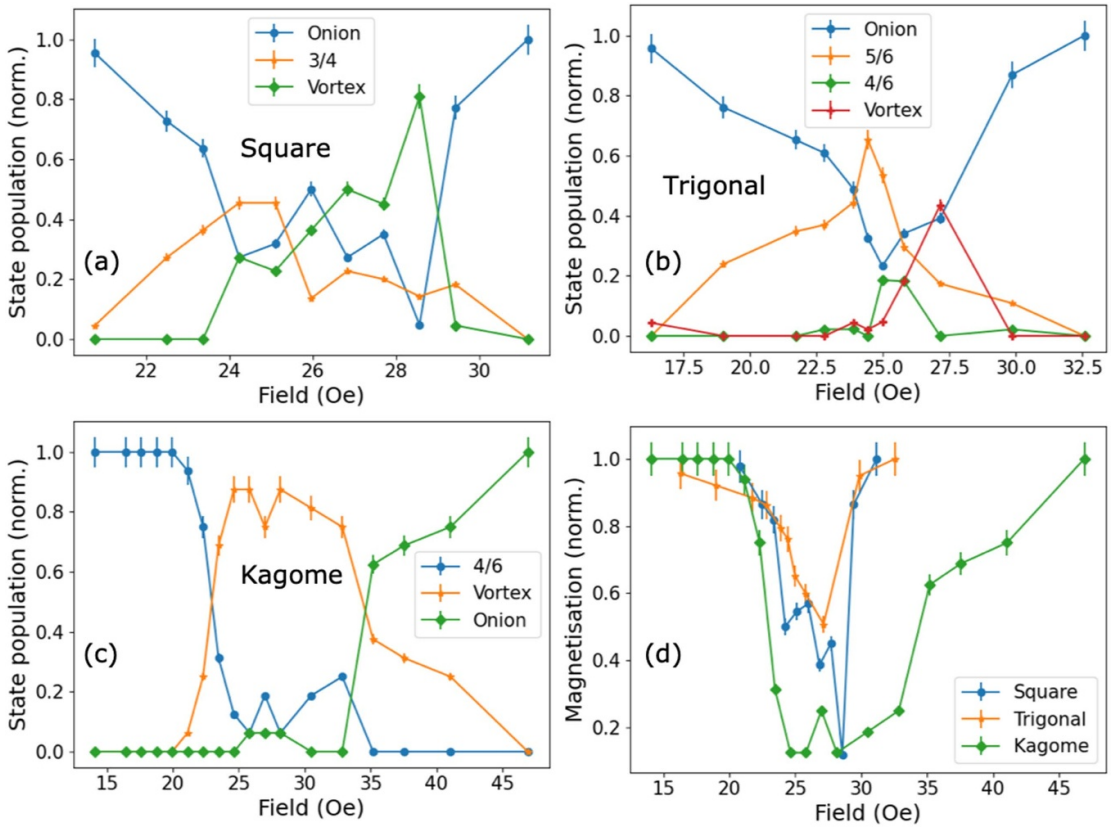

Figure 3. The magnetic state populations for the (a) square, (b) trigonal and (c) Kagome lattice NRAs as H_{rot} is varied. The magnetic states are schematically shown in figure 2. (d) The variation of the net magnetisation along the saturation direction with H_{rot} for the three lattice arrangements.

this re-population was complete and NRA was saturated with 'onion' states, which rotated coherently with the applied field (figure 2(a-iv)).

Field-dependent state populations for the square lattice are shown in figure 3(a). A strongly non-linear variation of the these was observed in the region of emergent dynamics, resulting in a plurality of MDW states, being observed at intermediate applied fields ($H_{rot} = 24 - 31$ Oe). The decrease in 'onion' states (between $H_{rot} = 20 - 24$ Oe) was accompanied by an increase in '3/4' states. The '3/4' states then gave way to a majority of 'vortex' states, the population of which continued to increase until they peaked at $H_{rot} = 29$ Oe. Further increases in field resulted in a relatively sharp re-population with 'onion' states. These behaviours were reflected in the variation of the NRAs net magnetisation (along the PEEM sensitivity direction) with field (figure 3(d)) which was significantly reduced in the emergent regime due to the large population of '3/4' and 'vortex' states.

The trigonal NRA exhibited significant differences in behaviour to the square array. This was to be expected as the increased number of nearest neighbour rings in these arrays (NN = 6) meant that the MDW motion was inhibited by a greater number of pinning sites, and the formation of interlocking 'vortex' states in triads of adjacent rings was inherently frustrated [31]. Following saturation the rings adopted configurations, which were broadly identical to the bi-domain 'onion' states observed in the square array (Figure 2(b-i)). As the applied field increased beyond the onset of MDW depinning ($H_{rot} = 24 - 27$ Oe), new microstates were formed by MDWs moving either one ('5/6') or two ('4/6') junctions around the rings. Notably, many less 'vortex' states were formed than in the square lattice, reflecting the inherent geometric frustration of the lattice (figure 2(b-ii, iii)). At higher fields still ($H_{rot} = 32$ Oe) the array was repopulated with 'onion' states in a similar manner to the square lattice (figure 2(a-iv)). Field-dependent state populations again showed strongly non-linear trends, with a progressive evolution from majority 'onion' to '5/6', then '4/6' to 'vortex' as MDW depinning became more likely, before an eventual re-saturation with 'onion' microstates when the field was strong enough to reliably overcome pinning at all junctions (figure 3(b)). The variation in net magnetisation was broadly similar to that observed in the square lattice, with a dip occurring at intermediate fields, but with dramatically reduced magnitude due to the comparatively low 'vortex' population in the trigonal array.

The Kagome NRA exhibited the simplest microstate behaviour of the three lattices studied. Following the saturation, rings adopted '4/6' states (figure 2(c-i)). These differed from the 'onion' state configurations observed post-saturation in the other lattices, as the lower symmetry of the Kagome lattice meant no two junction sites were directly opposite each other. As the applied field increased ($H_{rot} = 22 - 27$ Oe) almost all rings progressively fell into interlocking 'vortex' states, thus reaching the magnetic ground state of the array (figure 2(c-ii, iii)). This was enabled by the lower number of pinning sites in the Kagome lattice, which made it easier for MDW pairs to meet, and annihilate with each other. Notably, a much higher applied field ($H_{rot} = 47$ Oe) was required to fully re-populate the array with 'onion' states than in the other two geometries (figure 2(c-iv)). This was because the square and trigonal lattices always contained a residual population of MDWs that could assist with MDW repopulation, while these had to be nucleated from the ground state in the Kagome lattice. Plots of field-dependent microstate populations confirmed that the Kagome array showed the largest population of 'vortex' states of all three lattice geometries (figure 3(c)). This was also reflected in the array's net magnetisation, which reached lower values at intermediate fields than either of the other lattices (figure 3(d)).

Collectively, the analysis of microstates showed that the different lattices differed substantially in both the microstates they formed, and the way the populations of these varied with applied fields. The NRAs were always initialised by saturating them with a large magnetic field and then relaxing them to remanence, thus placing them in a configuration with a large number of DWs. The precise magnetic configuration was consistent for each NRA geometry, but depended somewhat on the lattice arrangement as seen in figure 2. Since all the NRAs were fabricated in the same deposition run, we do not expect any significant material differences in the array and attribute the varied microstate NRA behaviours to geometric variations in them. Such differences would be expected to result in differences in computational behaviour were they able to be accessed by a tractable readout mechanism. However, the net magnetisation data presented in figure 3(d) showed that when the average properties of the arrays were considered these differences became less profound. There, all three lattices showed a broadly similar non-linear trends, differing only in the magnitude and field scaling of their responses.

3.2. Macroscopic NRA behaviour

Having explored the detailed microstate behaviour of the arrays we then explored the responses that were accessible via magnetoresistance measurements, and were therefore device tractable.

The macroscopic electric responses of the NRAs were obtained using Au contacts on either side of the NRA (shown in the SEM micrograph in figure 5(b)). The AMR characterisation procedure was the following: The NRAs were initially saturated and relaxed which fully populated the NRAs with MDWs. Subsequently, 30 cycles of a rotating magnetic field at a frequency of 19 Hz, which were created by applying 90° phase shifted waveforms to the x and y axis electromagnet coils (figure 4(a)), were applied and the AMR signal was recorded (figure 4(b)). The FFT of the last 10 cycles of the AMR signal was then obtained and the amplitudes of the $f_1 = 19$ Hz (input field frequency) and $f_2 = 38$ Hz (2× input field frequency) components (marked in figure 4(c)) were extracted. This was repeated for different field amplitudes. As explained in our previous work [11], the f_1 component corresponded to pinned MDWs stretching and contracting as the applied field rotated relative to their internal magnetisation and the f_2 component corresponded to the irreversible DW propagation transitions around the rings.

The AMR responses of the different lattice arrangement NRAs are shown in figures 5(a) and (c). All the different lattice arrangements show maxima in the f_1 response which denote the onset of MDW movement. Similarly, the f_2 responses for all the lattice arrangements start with a slow increase in amplitude and show a sigmoidal form due to MDW movement in the NRA.

We initially explain the form of the AMR plots in figures 5(a) and (b) by considering the data for the square lattice. The prominent peak in the f_1 response (marked by P_2) at $H_{rot} \approx 25$ Oe also appears as a harmonic in the f_2 response. This marks the field at which some of the MDWs depin from junctions stochastically (after maximum distortion) and start propagating and therefore no longer show the periodic stretching and contraction that produces the f_1 response [11]. The prominent transition in the f_2 response occurs at the $H_{rot} \approx 29$ Oe (marked by P_3) and corresponds to MDWs progressively depinning and starting to move with the rotating field. There is a corresponding peak observed in the f_1 response at this transition which is smaller than the peak observed at P_2. The field regime between the 1st and 2nd peaks in the f_1 response is when a variety of the different microstates shown in the PEEM images are stochastically formed. The decrease seen in the amplitude of the f_2 response is due to the formation of 'vortex' states.

The data for the other lattice arrangements were broadly similar, with a few minor differences. The large peak in the f_1 response for the trigonal lattice occurs at $H_{rot} \approx 20$ Oe (marked by P_1 in figure 5(a)) suggesting a lower energy barrier for the MDWs to overcome to start propagation in the trigonal lattice. The smaller

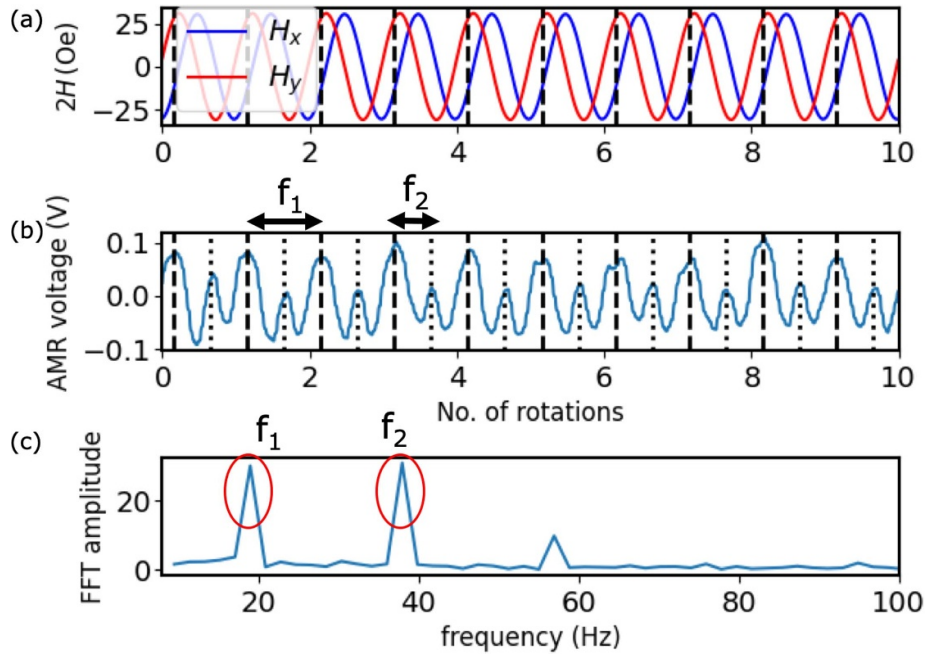

Figure 4. (a) The H_x and H_y components of the field profile that was applied to the sample and (b) the measured AMR signal for the first 10 rotations. (c) The Fourier transform of the signal with the f_1 and f_2 components marked.

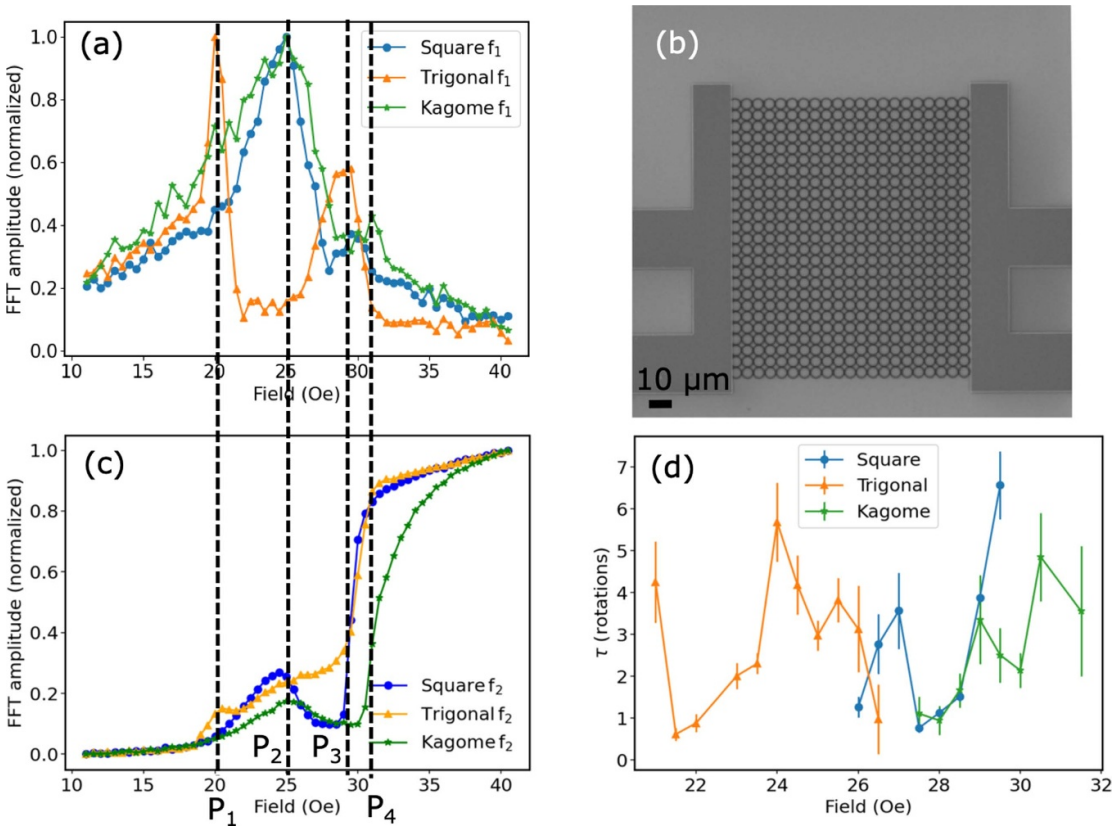

Figure 5. The (a) f_1 and (c) f_2 AMR responses as a function of H_{rot} show the different transitions in MDW dynamics in the NRAs. (b) An SEM micrograph of the square NRA showing the Au contacts used for the AMR measurements. (d) The time scales of settling for the different NRAs extracted from the AMR measurements.

peak in the f_1 response at $H_{rot} \approx 29$ Oe for the trigonal lattice (marked by P_3 and which correlated with the sharp transition in the f_2 response) is larger in amplitude compared to the same peak for the square and Kagome lattices. The sharp f_2 response transition for the Kagome lattice happens at a higher field of

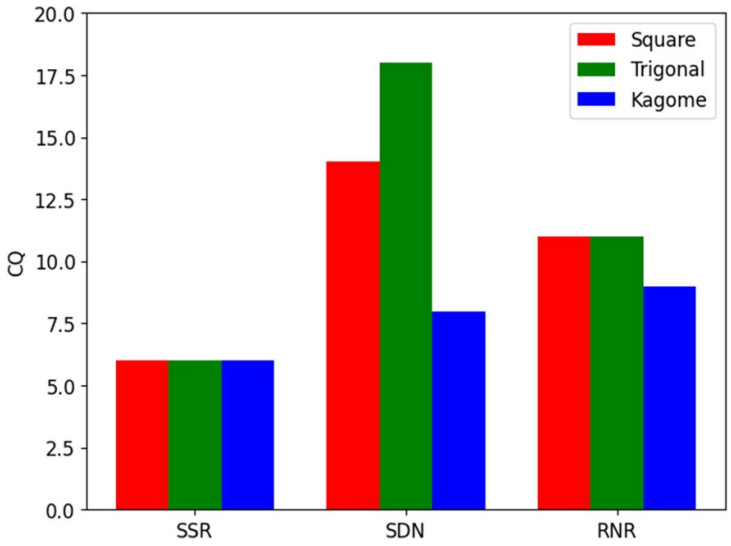

Figure 6. Comparison of peak computational quality (CQ) scores between each lattice arrangement for each of the the single subsample reservoir (SSR), single dynamical node (SDN), and rotating neurons reservoir (RNR) architectures.

$H_{rot} \approx 32$ Oe (marked by P_4) and is a consequence of the higher field required to repopulate the array with MDWs from the interlocking 'vortex' states as described above.

Thus we see that, as was observed for the magnetisation variation of the arrays, the differences between the AMR responses measured from the different latices are relatively minor; the features of the microstates seen in the state population variation of figures 3(a)–(c) do not manifest in the macroscopic ensemble AMR response of these arrays.

In addition to the non-linearity of its transfer function, the transient nature of a reservoir's dynamics is key to it is computational properties [4]. To understand these we also studied the time scales over which the NRAs' AMR signals settled at select field points.

In these measurements, the magnetisation of the array was again initially saturated and relaxed, creating MDWs at remanance. Then, 50 cycles of a rotating field was applied to the array and the AMR signal simultaneously recorded. The time constants (τ) were obtained by fitting an exponential dependence of the form $y = A\left(1 - e^{-\frac{x}{\tau}+B}\right)$ to the envelope of the AMR signal. Note that above and below these field values, the time constants could not be extracted. This was because at lower fields, the change in AMR signal was not appreciable and at higher fields, the signal settled into high amplitude oscillations (corresponding to propagating MDWs) by one field rotation. It was observed from figure 5(c) that all the lattice arrangements exhibit a similar range of maximum and minimum settling times.

Collectively the analysis of the AMR responses of the arrays show that, while the different lattice arrangements show clear differences in their microstate behaviours, global AMR measurements showed only slight variations in the global response of the NRAs, representing smaller perturbations on top of consistent general trends.

3.3. Computational evaluation of lattice arrangements

Having characterised the basic behaviours of the devices, we quantified the computational properties of the NRAs in each of the three lattice arrangements according to the metrics and architectures defined in section 2. Figure 6 plots the peak CQ metric score for each of the three lattice arrangements, with each of the three reservoir architectures. The plots of CQ for each lattice arrangement and architecture as a function of H_c and H_r can be found in the Supplementary material. The computational architectural choice is the dominant factor when determining the computational properties of the constructed reservoirs, with smaller variance in between the lattice arrangements for a given reservoir architecture. This implies that a change into the data input/output paradigm has a more significant effect on the computational properties of a reservoir than perturbing a device's response via geometric changes. It was only the SDN architecture that showed appreciable variation in CQ between the different lattice arrangements. CQ here is correlated with the number of states available for each ring within the three lattices: trigonal has the highest number of available states, and the highest metric score, while Kagome lattices have the fewest available states and the lowest metric scores, tying the greater computational complexity offered by the square and trigonal arrays to the greater microstate complexity available to these arrays. The poor CQ of the Kagome lattice is also likely

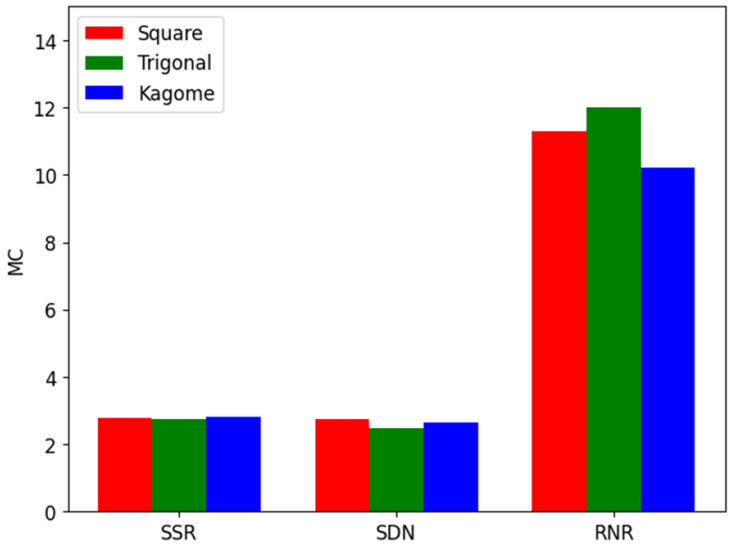

Figure 7. Peak memory capacity (MC) metric maps for the nine architecture/lattice arrangement pairs.

due to the increased tendency of Kagome lattices to form 'vortex' states compared to the other arrays, since the lack of mobile domain walls with increased 'vortex' states leads to a suppression the dynamic behaviours which the SDN architecture relies upon [11]. Overall, we observe that the SDN architecture both provides the highest CQ and is most expressive of array geometry, suggesting it is able to draw out the effects of microstate differences to some degree. CQ is typically lower for the RNR architecture, and is lower still for the SSR architecture.

Memory is another important computational property of reservoirs as it determines the timescale over which the reservoir responds to input and for how long information stays in the reservoir. This allows strong performance in time-series analysis tasks if the timescales of the task are well-matched to the timescales of the reservoir [32]. Figure 7 shows the peak linear MC obtained for the different lattice and architecture combinations. The plots of MC for each lattice arrangement and architecture as a function of H_c and H_r can be found in the SI. Once again we observe that reservoir architecture had a much more profound effect on computational properties than lattice arrangements, with the RNR providing the highest degree of memory and the square and trigonal arrays performing slightly better than the Kagome lattice in this architecture (due to the relative lack of complexity in the behaviour of the Kagome NRA). This is due to the ability of the RNR architecture to store information across the distinct real nodes, whereas the single/virtual nodes in the SSR and SDN will have information washed out of the node as more inputs are provided.

While the task-independent metrics KR, GR, and CQ provide a good means for comparing between similar reservoir initialisations, many design choices and experimental factors can make direct comparisons between different devices difficult. For example, past studies have shown stark differences between calculated metrics for nominally similar nodes depending upon their input/and output granularity from binary to analogue input/outputs [24], the filtering of noise [33], or the number of output nodes which acts as a hard bound for KR and GR [25]. However, to provide context, the 'peak' metric scores listed here (32 output nodes for SSR, 50 for SDN/RNR, all analogue inputs and outputs) can be tentatively compared with simulations of spintronic systems in the literature, such as a CQ of 7 for spin-wave interference based RC with 20 nodes with analogue input/output [34], and a CQ of 130 for an artificial spin ice with 220 nodes for binary inputs but analogue readouts [27]. We note however that the above are simulation studies, rather than experimental measurements as we present here. Furthermore, the improved CQ measured on the trigonal lattice arrangement outperformed those obtained for the square lattices used in previous studies [11, 19].

Memory capacity also has a range of similar factors that complicate comparions with other systems, such as the size of the network, with more nodes leading to greater memory capacities (with diminishing returns) [26], whether analogue or binary inputs are recalled (with analogue inputs being more difficult), whether delayed feedback is used to increase temporal dependencies of the network, and whether studies are done experimentally or numerically. For comparison, numerical studies of a time-multiplexed spin-torque nano oscillator showed memory capacities of 3.29 with binary inputs and 50 virtual nodes [35], while arrays of oscillators had memory capacities of 15 for binary inputs and 50 distinct nodes [36]. Experimental demonstrations with spin-torque nano oscillators in a time-multiplexed arrangement with 200 nodes and

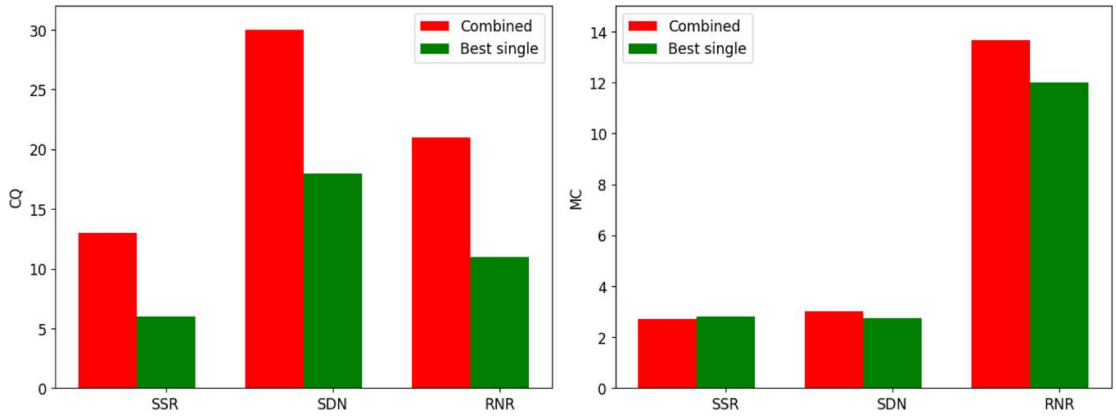

Figure 8. Comparison between peak performances of the combined networks (red) and the highest performing single network (green) for both computational quality (CQ) and memory capacity (MC).

binary inputs showed memory capacities of 1.8 [37]. Here, the NRAs rivalled the memory capacities observed in simulations using binary inputs, with experimentally gathered data and with analogue inputs.

3.4. Combining lattice outputs

Whilst the lattice arrangements showed slight differences in terms of maximum scores achieved in metrics, they often showed considerable differences in the input scaling parameters at which these areas of peak performance were reached, implying different behaviours in different lattices at a given applied field. This enabled multiple behaviours to be captured at a given H_c and H_r by combining the different lattices' responses. To show the difference in computational properties resulting from the combination of the lattice arrangements, the metric calculations were repeated with the output for each lattice concatenated together to form a single reservoir state matrix with three times as many outputs per input.

Figure 8 shows the resulting peak CQ and MC values compared to the best performing single lattice/architecture pair for the three reservoir architectures. It can be observed that there was a considerable increase in the CQ for all three reservoir architectures compared to the best performing single case for a given architecture. This is due to the different nonlinear representations provided by each lattice providing better ability to separate/generalise data. When considering MC, the combined reservoirs performed similarly in terms of peak score. For the SSR and SDN cases, this is likely tied to the inability to store information beyond 2 inputs in any of the lattices in a single node/single time multiplexed node configuration. There is slight improvement for the RNR, likely due to the presence of varied timescales for the three lattices as shown in figure 5(d).

Figure 9 shows the metric heatmaps of the combined reservoir. There is a broadening of the optimal regions of operation compared to the single lattices (refer to heat maps in the SI) due to the different ranges of activity of each lattice arrangement, ensuring at least one is operating in a dynamically interesting regime for a broader range of input scaling parameters. This highlights the potential scalability of the NRAs in terms of expanding computational capability via geometrical manipulation, as improved CQ is obtained when combining the different nonlinear relationships between input and output provided by each of the different lattice arrangements. Similar expansion of the range of computational properties available at a given input scaling are expected for other RC platforms, providing that their dynamic properties can be manipulated into different dynamical regimes for a given input stimuli via geometrical manipulation. Combining the outputs also provides a means of exploiting the different timescales of response from the three lattice arrangements highlighted in figure 5(d). This behaviour is functionally similar to the unconnected hierarchical ESNs presented in [38], which showed improvement in solving tasks on data with multiple timescales of auto-correlation.

4. Conclusions

In conclusion, we have studied the effects of lattice geometry and time-multiplexed reservoir architecture on the computational properties of magnetic nanoring array reservoir computers. High-resolution XPEEM measurements showed that the different lattices showed a wide variety of microscopic magnetic states, and different evolution of states with applied stimulus. However, when the computational capabilities of the arrays were measured via their AMR responses, similar computational metric scores were observed within a

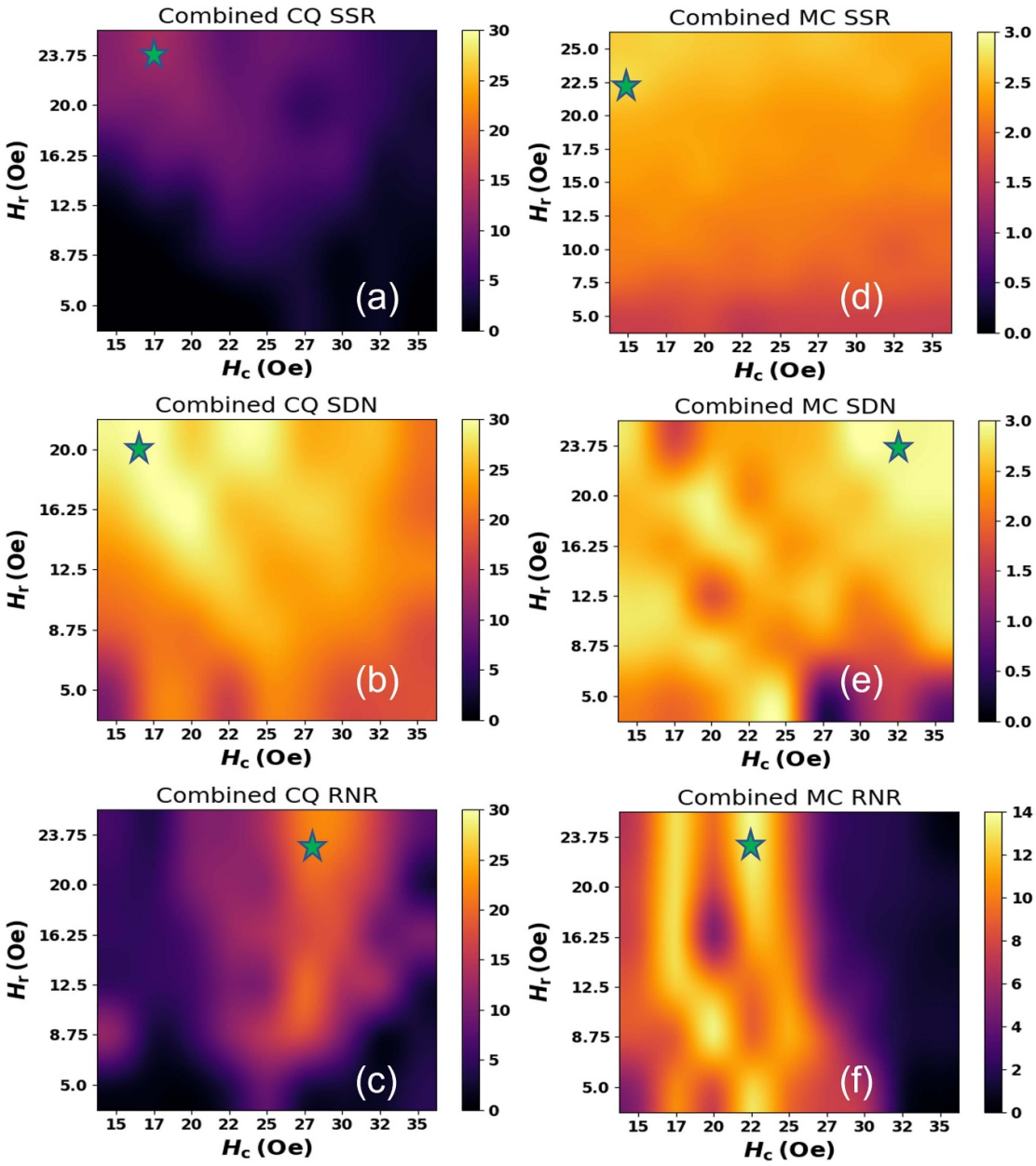

Figure 9. The memory capacity metric maps as a function of the centre field (H_c) and field range (H_r) for the SSR (a)–(c), SDN (d)–(f) and RNR (g)–(i) RC architectures for the different lattice arrangements. The stars mark the regions where maxima are observed.

given reservoir architecture, highlighting the role of array-wide measurements in obscuring the different microstate behaviours. This suggests that the manner with which external information is interfaced with the dynamical system, such as time-multiplexing of information, is more significant for determining computational properties than the exact response of the dynamical system itself. In spite of this, the ability to exploit different dynamical regimes between the lattices at a given field allowed improved computational performance when the different lattices were combined. These conclusions are likely to extend to different physical systems whose responses to input stimuli can be perturbed via geometric manipulations.

Collectively, our measurements show that although the different lattice arrangements have considerably different microstate responses (resembling considerably different underlying physical mechanisms of node response), global 1D measurements of array state such as AMR provide limited differences in computational behaviour due to minor differences between readouts of the state of the system (similar to slight manipulation of the activation functions of nodes in conventional RC).We therefore surmise that the use of global readouts for assessing computational performance of the NRAs mask some of the complex variations in physical behaviours imaged in the NRAs, and evidences potential paths for improvements in readout strategies.

In order to exploit the microstate differences observed between the lattice arrangements, we anticipate that coupling local inputs of data (via Oersted fields from current carrying microstrip lines, or spin-orbit torque induced DW propagation) with spatially-sensitive readouts of state would allow for better exploitation of the spatially-distributed responses observed in the NRAs. Additionally, a measurement technique such as ferromagnetic resonance [12] can be used in which the measured spin-wave spectrum can help resolve the microscopic MDW configuration and thus be sensitive to spatial information configuration of the NRA. For other physical systems with spatially-distributed responses, it will be similarly important to develop measurement techniques that can capture these differences.

Data availability statement

The data that support the findings of this study are openly available at the following URL/DOI: https://doi.org/10.15131/shef.data.24785883.

Acknowledgments

We acknowledge funding from the Horizon 2020 FET-Open SpinEngine (Agreement No 861618) and the EPSRC MARCH Project EP/V006339/1 and EP/V006029/1. M A N and M F acknowledge funding from the Spanish MICIN through Grant PID2021-122980OB-C54. We would like to acknowledge R Allenspach and A Bischoff of IBM Zurich for useful discussions.

ORCID iDs

G Venkat https://orcid.org/0000-0001-6255-3151
C Swindells https://orcid.org/0000-0002-9572-5930
S Stepney https://orcid.org/0000-0003-3146-5401

References

[1] Spherical Insights 2023 Global neuromorphic computing market size (available at: www.sphericalinsights.com/reports/neuromorphic-computing-market) (Accessed 13 June 2023)
[2] Jaeger H 2001 *Bonn, Germany: German National Research Center for Information Technology GMD Technical Report* vol 148 p 13
[3] Lukoševičius M, Jaeger H and Schrauwen B 2012 *KI-Küns. Intell.* **26** 365–71
[4] Allwood D A *et al* 2023 *Appl. Phys. Lett.* **122** 040501
[5] Tanaka G, Yamane T, Héroux J B, Nakane R, Kanazawa N, Takeda S, Numata H, Nakano D and Hirose A 2019 *Neural Netw.* **115** 100–23
[6] Paquot Y, Duport F, Smerieri A, Dambre J, Schrauwen B, Haelterman M and Massar S 2012 *Sci. Rep.* **2** 287
[7] Dion G *et al* 2021 *Reservoir Computing: Theory, Physical Implementations and Applications* (Springer) pp 191–217
[8] Mehonic A Sebastian A, Rajendran B, Simeone O, Vasilaki E and Kenyon A J 2020 *Adv. Intell. Syst.* **2** 2000085
[9] Kulkarni M S and Teuscher C 2012 Memristor-based reservoir computing *Proc. 2012 IEEE/ACM Int. Symp. on Nanoscale Architectures* pp 226–32
[10] Dale M, Stepney S, Miller J F and Trefzer M 2017 Reservoir computing in materio: an evaluation of configuration through evolution *2016 IEEE Symp. Series on Computational Intelligence, SSCI 2016* (Institute of Electrical and Electronics Engineers Inc.)
[11] Vidamour I *et al* 2023 *Commun. Phys.* **6** 230
[12] Gartside J C, Stenning K D, Vanstone A, Holder H H, Arroo D M, Dion T, Caravelli F, Kurebayashi H and Branford W R 2022 *Nat. Nanotechnol.* **17** 460–9
[13] Larger L, Baylón-Fuentes A, Martinenghi R, Udaltsov V S, Chembo Y K and Jacquot M 2017 *Phys. Rev.* X **7** 011015
[14] Canaday D, Griffith A and Gauthier D J 2018 *Chaos* **28** 123119
[15] Wang C, Adeyeye A and Singh N 2006 *Nanotechnology* **17** 1629
[16] Skjærvø S H, Marrows C H, Stamps R L and Heyderman L J 2020 *Nat. Rev. Phys.* **2** 13–28
[17] León A 2013 *Curr. Appl. Phys.* **13** 2014–8
[18] Dawidek R W *et al* 2021 *Adv. Funct. Mater.* **31** 2008389
[19] Vidamour I T *et al* 2022 *Nanotechnology* **33** 485203
[20] Bordignon G, Fischbacher T, Franchin M, Zimmermann J P, Zhukov A A, Metlushko V V, de Groot P A J and Fangohr H 2007 *IEEE Trans. Magn.* **43** 2881–3
[21] Ross C, Castaño F J, Morecroft D, Jung W, Smith H I, Moore T A, Hayward T J, Bland J A C, Bromwich T J and Petford-Long A K 2006 *J. Appl. Phys.* **99** 08S501
[22] Foerster M, Prat J, Massana V, Gonzalez N, Fontsere A, Molas B, Matilla O, Pellegrin E and Aballe L 2016 *Ultramicroscopy* **171** 63–69
[23] Venkat G *et al* 2021 Peem-data-analysis (available at: https://gitlab.com/spintronic-computing-group/data-analysis/peem-data-analysis)
[24] Büsing L, Schrauwen B and Legenstein R 2010 *Neural Comput.* **22** 1272–311
[25] Dale M *et al* 2019 *Proc. R. Soc.* A **475** 20180723
[26] Jaeger H 2002 Short term memory in echo state networks *Technical Report* (GMD Report 152)
[27] Jensen J H and Tufte G 2020 *Reservoir Computing in Artificial Spin Ice* (MIT Press) pp 376–83
[28] Appeltant L, Soriano M C, Van Der Sande G, Danckaert J, Massar S, Dambre J, Schrauwen B, Mirasso C R and Fischer I 2011 *Nat. Commun.* **2** 468
[29] Liang X *et al* 2022 *Nat. Commun.* **13** 1549

[30] Negoita M, Hayward T J and Allwood D A 2012 *Appl. Phys. Lett.* **100** 072405
[31] Rose V, Buchanan K, Chung S-H, Grimsditch M, Metlushko V, Hoffmann A, Novosad V, Bader S D and Ibach H 2006 *Phys. Rev.* B **73** 094442
[32] Lukoševičius M and Jaeger H 2009 *Comput. Sci. Rev.* **3** 127–49
[33] Danilenko G, Kovalev A, Viktorov E, Locquet A, Citrin D and Rontani D 2023 *Chaos* **33** 013116
[34] Papp A, Csaba G and Porod W 2021 *Appl. Phys. Lett.* **119** 112403
[35] Taniguchi T, Ogihara A, Utsumi Y and Tsunegi S 2022 *Sci. Rep.* **12** 10627
[36] Kanao T, Suto H, Mizushima K, Goto H, Tanamoto T and Nagasawa T 2019 *Phys. Rev. Appl.* **12** 024052
[37] Tsunegi S, Taniguchi T, Miwa S, Nakajima K, Yakushiji K, Fukushima A, Yuasa S and Kubota H 2018 *Jpn. J. Appl. Phys.* **57** 120307
[38] Manneschi L, Ellis M O A, Gigante G, Lin A C, Del Giudice P and Vasilaki E 2021 *Front. Appl. Math. Stat.* **6** 616658